Differential spatial regulation and activation of integrin nanoclusters inside focal adhesions.

Sarah Keary[1†‡], Nicolas Mateos[1], Felix Campelo[1], and Maria F. Garcia-Parajo[1,2*]

[1] *ICFO – Institut de Ciencies Fotoniques, The Barcelona Institute of Science and Technology, 08860 Castelldefels (Barcelona), Spain.*

[2]*ICREA, Pg. Lluís Companys 23, 08010 Barcelona, Spain.*

Corresponding author:

* Maria F. Garcia-Parajo: maria.garcia-parajo@icfo.eu

Present address:

[†]Institut Curie, Centre de Recherche, 75248 Paris, France;

[‡] Centre National de la Recherche Scientifique, Unité Mixte de Recherche 168, 75248 Paris, France;

Abstract

$\alpha_5\beta_1$ and $\alpha_v\beta_3$ integrins are core components of focal adhesions (FAs) involved in cell attachment, migration and mechanobiology-dependent processes. Recent works indicate that both integrins organize in nanoclusters inside FAs, with sub-populations of active and inactive β_1 nanoclusters. However, whether both integrins work in concert or their activities are spatially regulated is not fully understood. Using dual-color super-resolution microscopy we show that integrins $\alpha_5\beta_1$ and $\alpha_v\beta_3$ exhibit similar functional nanoscale segregation. Notably, both integrins never mix at the nanoscale indicating that their functions might be spatially regulated. We find a nearly 1:1 stoichiometry between active integrin and adaptor nanoclusters suggesting that coordinated integrin activation occurs via the concurrent engagement of adaptor nanoclusters. Interestingly, $\alpha_5\beta_1$ nanoclusters preferentially localize at the FA periphery in close proximity to adaptor nanoclusters, establishing regions of multi-nanocluster enrichment, whereas $\alpha_v\beta_3$ nanoclusters uniformly distribute throughout FAs. Overall, our results show that adhesion proteins arrange as modular nanoscale units that distinctively organize inside FAs to spatially regulate integrin activation and function.

Introduction

Adhesion complexes (ACs) in adherent cells, such as focal adhesions (FAs) and fibrillar adhesions (fAs) are places for cell attachment, mechanosensing and mechanotransduction (1–4). These structures are composed by different integrin receptors that bind to their ligands on the extracellular matrix (ECM), and by a myriad of intracellular adaptors, proteins that dynamically connect integrins to the actin cytoskeleton machinery relaying the transmission of mechanical forces in a bidirectional manner (5–7). Studies over the last two decades have provided a wealth of information focused on understanding these complexes, the proteins they contain, their role in cellular processes, such as mechanosensing, migration and proliferation, as well as how influential their regulation is in developmental and pathogenic processes (8–15).

Integrins $\alpha_5\beta_1$ and $\alpha_v\beta_3$ are transmembrane heterodimeric proteins critical for the formation of ACs. Both $\alpha_5\beta_1$ and $\alpha_v\beta_3$ bind to the RGD peptide motif of certain ECM components, such as fibronectin (16–18), and are linked to the cell's cytoskeleton via many of the same adaptor proteins (19–22). The apparent redundancy of different integrins binding to the same ligand and same adaptor proteins is intriguing and has been the subject of intense research over the past years. Earlier studies on primary fibroblasts showed that these integrins segregate in different adhesion structures, indicating different roles, with $\alpha_5\beta_1$ being enriched in fAs (23), adhesive sites at central regions of the cell, and $\alpha_v\beta_3$ being confined to focal complexes at the base of cellular protrusions, and to FAs, which anchor contractile stress fibers at the periphery of the cell (24). However, more recent super-resolution microscopy studies showed that both types of integrins are simultaneously present inside FAs (25). Within FAs, $\alpha_5\beta_1$ has been proposed as the integrin responsible for adhesion strength while $\alpha_v\beta_3$ enables mechanotransduction, as cells exposed to $\alpha_5\beta_1$ blocking antibody exhibited weaker attachment than those whose $\alpha_v\beta_3$ integrins were blocked (5). These results are also aligned to *in vitro* reconstitution experiments, that have assessed the catch-bond behavior of both integrins with fibronectin. In this type of bond, the lifetime of the bond increases as the applied force increases, up to a certain threshold, beyond which the bond ruptures. The rupture force for $\alpha_5\beta_1$ binding to its ligand has been found to be higher (~10–30 pN) than that of $\alpha_v\beta_3$ (~5–25 pN) (26, 27). Nevertheless, single molecule tracking data indicated that $\alpha_v\beta_3$ integrins are mainly stationary inside FAs and more stably bound to the ligand, favoring adhesion as its main role (25). It has been also shown that $\alpha_5\beta_1$ is involved in Rho activation during late spreading, enhancing RhoA-mediated actomyosin contractility (24, 28), supporting the idea that $\alpha_5\beta_1$ is

65 involved in force-mediated adhesion reinforcement. In a *tour-de-force* effort, Fässler and colleagues found that only the simultaneous expression of both integrins enabled cells to sense the rigidity of the ECM and to respond by reinforcing the actomyosin structure (29). These results, supported by others (30), have led to the recent notion that both integrins work in a synergistic manner, exhibiting cooperativity during cell adhesion, migration and
70 mechanosensing, although the mechanisms are far from being fully resolved (30).

The highly dynamic conformational states exhibited by integrins together with their lateral and axial nanoscale organization might play important roles regulating the differential or synergistic functions of different integrins inside FAs. Indeed, it has been shown that integrins can rapidly transition between different conformational states that relate to their activation and
75 binding capacity to their ligands (25, 31, 32). Moreover, in addition to the nanoscale axial segregation of different AC components inside FAs (33), it has been reported that integrins as well as different adaptor proteins also segregate laterally into small nanoclusters inside FAs (34–37). Recent super-resolution studies have further shown that β_1 integrins segregate in both active and inactive nanoclusters inside FAs (36) and single-molecule tension measurements
80 uncovered distinct sub-populations of load bearing integrins and a high fraction of unengaged integrins (38, 39). Together, these results suggest that at any given time only a fraction of integrins might be active inside FAs and engaged with their adaptor partners. Such a dynamic scenario would allow integrins to differentially interact with their environment and possibly diversify their functions. As $\alpha_5\beta_1$ and $\alpha_v\beta_3$ have different activation states and are both
85 contained in FAs, it is plausible that their spatial regulation and activation state inside FAs provides a physical mechanism to tune their functions. However, such studies have not been reported yet.

Here, we combined dual-color super-resolution microscopy together with robust analytical tools to study a number of endogenous FA proteins on human fibroblast cells. Specifically, we
90 imaged one of the two integrins ($\alpha_5\beta_1/\alpha_v\beta_3$), their full population or active conformations, with each of three key adaptors proteins, paxillin, talin and vinculin. Our results show that each of these proteins form segregated nanoclusters of remarkably similar size and molecular density inside FAs, and interestingly, also on the membrane outside of ACs. Moreover, we find sub-populations of active and inactive β_1 and β_3 nanoclusters inside FAs, which spatially segregate
95 from each other and provide evidence for a nearly 1:1 stoichiometry between talin, vinculin and active integrin nanoclusters. Interestingly, we find that $\alpha_v\beta_3$ nanoclusters organize randomly inside FAs regardless of their activation state, whereas $\alpha_5\beta_1$ and in particular the active conformation of β_1 nanoclusters preferentially organize at the edges of FAs. Overall, we

propose that the nano- and meso-scale organization of $\alpha_5\beta_1$ and $\alpha_v\beta_3$ integrins and their distinct
100 lateral segregation and activation state are key factors in the differentiation of their roles within FAs.

Results

Proteins of the ACs organize as universal nanoclusters across regions of the basal membrane.

105 We employed dual-color super-resolution microscopy based on stochastic optical reconstruction microscopy (STORM) to determine how adhesion proteins (integrins and key adaptor proteins) are spatially organized at the nanoscale. Human fibroblasts (HFF-1 cells) were seeded on fibronectin (FN)-coated glass slides for 24 h, after which the cells were processed for immunofluorescence. One integrin (either the total population of $\alpha_5\beta_1$ or $\alpha_v\beta_3$, or
110 the active population specific to the β_1 or β_3 integrin subunit) was labeled together with one adaptor protein (paxillin, C terminus of talin-1, or vinculin) and then imaged using STORM. We note that while the pan antibodies used to target the full population of integrins are specific to $\alpha_5\beta_1$ or $\alpha_v\beta_3$, (with the anti-α_5 antibody binding the α_5 subunit, which only dimerizes with β_1, and the anti-$\alpha_v\beta_3$ targeting this specific heterodimer), the active antibodies target the β
115 subunits. These β subunits can dimerize with other α subunits, but with our experimental conditions, where FN is the most abundant ligand (see Materials & Methods), the primary integrins being probed are the heterodimers, $\alpha_5\beta_1$ or $\alpha_v\beta_3$. Given the huge number of adaptor proteins that have been reported to interact with integrins (19, 20), we chose for paxillin, talin and vinculin since they belong to the core-components of the adhesome (21) and crucially
120 locate at distinct axial layers of functional activity, i.e., paxillin at the signaling layer, while talin and vinculin locate at the force-transduction layer (33).

Super-resolution images qualitatively revealed an inhomogeneous distribution for all the proteins examined, forming small and laterally segregated nanoclusters inside FAs (Fig. 1A–D). To quantitatively substantiate these observations, we first used a mask to classify all the
125 single molecule localization events according to their location on the membrane, i.e., FAs, fAs or outside ACs (see Materials & Methods, Fig. S1A-F). To group localizations into nanoclusters we used a density-based spatial clustering of applications with noise (DBSCAN) algorithm (40), which has been extensively used for quantifying protein nanoclustering from single molecule localization images, including β_1 integrins inside FAs (36, 41). Since STORM
130 data consist of lists of single-molecule localizations and each labeled protein can be localized multiple times due to fluorophore blinking (42), it is important to first assess the number of

localizations detected due to the multiple blinking events of a single fluorophore. For this, we followed an approach similar to that reported by Spiess et al. to generate distributions of the number of localizations obtained from isolated fluorescent spots on glass next to the cells, for both channels, these will mostly correspond to individual antibodies (Abs) (Fig. 1E, Materials & Methods). By doing this approach one can determine the number of localizations corresponding to individual Abs and infer whether the clustered localizations observed correspond to individual or multiple proteins. The median values of the distributions were 5 localizations for Alexa 405-Alexa 647-conjugated Abs (Channel 1) and 3 localizations for Cy3–Alexa 647-conjugated Abs (Channel 2). Moreover, to further minimize the effect of fluorophore blinking on cluster identification, we imposed a threshold of 10 localizations as commonly used in the field (36, 41). Thus, any cluster identified by DBSCAN with 10 or more localizations was considered as a cluster of more than one protein (see Materials & Methods). DBSCAN classified between 70% to 80% of the localizations of each of the proteins as belonging to nanoclusters, regardless of whether they were located inside FAs or on regions of the membrane outside ACs (Fig. S1G-I). Notably, the number of localizations per nanocluster and their size were similar across the different adhesion proteins (integrins and adaptors) inside FAs, with a median of ~20 localizations per nanocluster, likely corresponding to a few copies of the protein, and a diameter of ~ 40–45 nm (Fig. 1F, G).

Similar results in terms of size and number of localizations per nanocluster were obtained when performing the analysis outside ACs (Fig. S2). In addition, the nanocluster characteristics were maintained when specifically labeling the active integrin (β_1 or β_3) populations (Fig. 1 D, F, G). These results are in good quantitative agreement with previous reports using STORM showing that both active and inactive integrin β_1 nanoclusters have a median size of 40 nm and 35 nm, respectively, as well as comparable number of single molecule localizations per nanocluster (36). Overall, our results agree with previous work on $\alpha_5\beta_1$ and provides new insight on the integrin $\alpha_v\beta_3$ and the main adaptor proteins, paxillin, talin and vinculin, indicating that organization into laterally segregated nanoclusters of similar size and number of molecules is maintained across different protein types. Interestingly, such nanoscale organization is independent of whether these adhesion proteins partition inside FAs or outside ACs (Fig. S2).

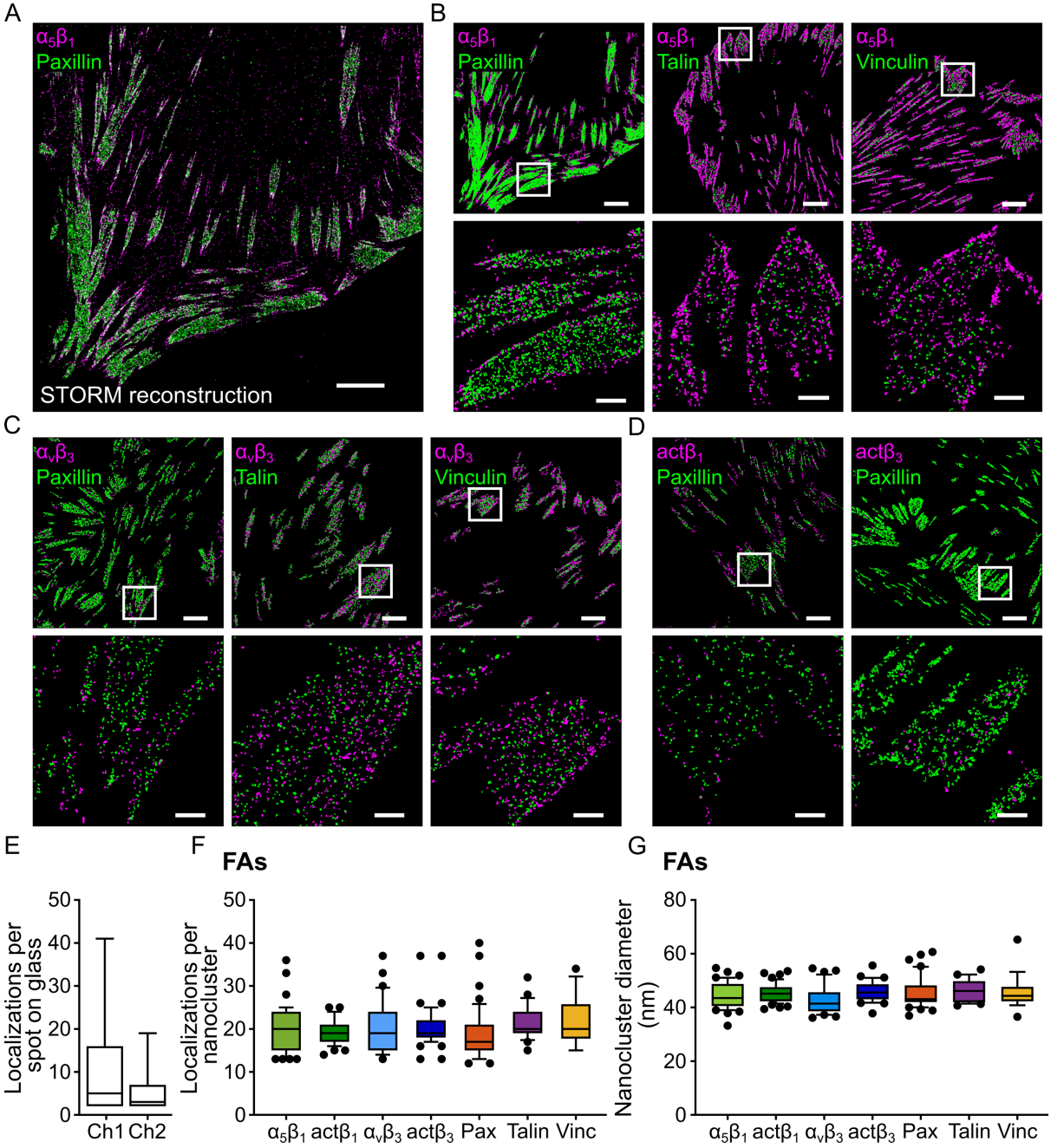

Figure 1 **Proteins of FAs organize as universal nanoclusters of similar size and containing a similar number of proteins.**

(A) Representative dual-color STORM image of an HFF-1 cell fixed after 24 h on FN and labeled for $\alpha_5\beta_1$ (magenta) and paxillin (green). Scale bar: 5 µm. (B) Representative images of all the adhesions identified for $\alpha_5\beta_1$ with paxillin (left), talin (middle) and vinculin (right), with zoomed-in regions shown below each panel. Scale bar top row: 5 µm, bottom row: 1 µm. (C) Representative images of all the adhesions identified for $\alpha_v\beta_3$ with paxillin (left), talin (middle) and vinculin (right), with zoomed-in regions shown below each panel. Scale bar top row: 5 µm, bottom row: 1 µm. (D) Representative images all the adhesions identified for of active β_1 (act β_1) with paxillin (left), active β_3 (act β_3) with paxillin (right), with zoomed-in regions shown below each panel. Scale bar top row: 5 µm, bottom row: 1 µm. (E) Distribution for the number of localizations per secondary antibody on glass next to cell regions for both of the secondary antibodies used in this study, goat anti-mouse Alexa 405–Alexa 647 (Ch1) and goat anti-rabbit Cy3–Alexa 647 (Ch2). The median number of localizations per spot corresponds to: 5 for Alexa 405-Alexa 647-conjugated antibodies and 3 for Cy3–Alexa 647-conjugated antibodies (see Materials & Methods). (F, G) Box-and-whisker plots showing the number of localizations per

nanocluster (F) and the nanocluster diameter (G) for the proteins in this study. The box represents the range from the 25th to the 75th percentiles and whiskers from 10th to 90th percentiles, with the median indicated by a horizontal line. Points outside these whiskers correspond to outliers. Individual points (points within the whiskers not shown) correspond to the median value over all nanoclusters for each cell (for N values, i.e., number of independent experiments, see SI Table S5). No statistical differences were found using the multi comparison one-way ANOVA test, where not significant (ns) corresponds to p>0.05.

Global mesoscale organization of adhesion protein nanoclusters inside FAs.

We next sought to investigate how the different adhesion proteins laterally organize inside FAs beyond their nanoclustering, i.e., at the mesoscale. For this, we first quantified the density of nanoclusters per unit area of the membrane, within FAs (Fig. 2A) and outside ACs (Fig. 2B). As expected, the density of nanoclusters was larger in FAs as compared to outside adhesions (~5–10-fold increase) (Fig. 2A, B). Adaptor proteins, such as talin or vinculin, are shared between $\alpha_5\beta_1$ and $\alpha_v\beta_3$ integrins (21), therefore we compared the density of the full population of integrin nanoclusters (~36 μm^{-2} in FAs) to the density of adaptor protein nanoclusters (~10–12 μm^{-2} for talin and vinculin, ~20 μm^{-2} for paxillin in FAs). These data reveal a significantly higher (~2–4 fold) density of integrin nanoclusters in comparison to their adaptors and, consequently, a stoichiometric nanocluster mismatch between the integrins and the adaptors, regardless of whether they partition inside or outside FAs (Fig 2A, B). Since the active integrin conformation is the one engaged with the adaptors (43, 44), we also quantified the density of active integrin nanoclusters (active β_1 and active β_3) per unit area inside FAs. Our results revealed that only ~ 30% of the total $\alpha_5\beta_1$ nanocluster population were in an active conformation, and this percentage was even lower for β_3 nanoclusters (~ 20%) (Fig. 2A), indicating that at any given time there is a large percentage of inactive integrin nanoclusters inside FAs. We note that these percentages might be even lower considering that our Abs for mapping the active conformations are not exclusive for $\alpha_5\beta_1$ and $\alpha_v\beta_3$, but rather to the total active β_1 and β_3 sub-populations. Notably, the total density of active β_1 and β_3 integrin nanoclusters stoichiometrically matches that of talin and vinculin nanoclusters, and it is only slightly outnumbered by paxillin nanoclusters inside FAs (Fig. 2A), suggesting that these active integrins might be fully engaged to their adaptors. The modest percentage of active β_1 integrin nanoclusters observed in our data (~ 30%, Fig. 2A) is in close agreement with a recent report from Spiess *et al*, obtained using a different super-resolution technique (36) and consistent with the high percentage of low-force bearing integrins measured by using single-molecule force sensors (39). In addition to the $\alpha_5\beta_1$ results, our data also reveal the existence of a sub-population of active β_3 nanoclusters inside FAs (Fig. 2A). Together, these results strengthen

the hypothesis proposed by Spiess et al. of a coordinated mechanism that laterally segregates active and inactive nanoclusters inside FAs (36).

Interestingly, despite this common feature, we found a significantly higher density of $\alpha_5\beta_1$ nanoclusters as compared to $\alpha_v\beta_3$ (Fig. 2A, B). Moreover, the percentage of active β_1 integrin nanoclusters was larger than for active β_3, in particular inside FAs (30% and 20% for active β_1 and active β_3, respectively) (Fig. 2A). To further enquire whether both types of integrin nanoclusters act in concert by associating at the nanoscale and sharing their vinculin and talin partners, we performed dual color STORM imaging of the total populations of $\alpha_5\beta_1$ and $\alpha_v\beta_3$ integrins (Fig. 2C). For this, we used a rabbit anti-α_5 antibody (see SI, Table S2) to enable simultaneous labeling with the mouse anti-$\alpha_v\beta_3$ antibody that we used throughout this study. Visual inspection as well as quantification of the images show that $\alpha_5\beta_1$ and $\alpha_v\beta_3$ do not intermix at the nanoscale, forming distinct nanoclusters that spatially segregate from each other inside FAs (Fig. S3A, B). The differences in expression levels, activation states, and lateral nano- and meso-scale segregation of $\alpha_5\beta_1$ and $\alpha_v\beta_3$ suggest the existence of a mechanism that defines the distinct functional roles of these two integrins inside FAs.

To get a better understanding on the global organization of both types of integrins in relation to their main adaptor proteins, we calculated the edge-to-edge distance between the nearest-neighbor integrin nanoclusters and each of the adaptors (see Materials & Methods). Although visual inspection of the dual color STORM images already suggested that integrin nanoclusters are also physically segregated from their adaptor partners (Fig. 1B, C) we used this quantitative approach to estimate the degree of colocalization (i.e., spatial overlap) between different nanoclusters. Since we measure edge-to-edge distances between nearest nanoclusters (EED-NN), values below zero correspond to physically overlapping nanoclusters, EED-NN values above zero to spatially segregated nanoclusters, and EED-NN = 0 corresponds to contiguous nanoclusters, i.e., next to each other. Our results quantitively confirm that the large majority of $\alpha_5\beta_1$ and $\alpha_v\beta_3$ nanoclusters are laterally segregated from their adaptor partners (Fig. 2D, Fig. S3C, D). Their spatial segregation is essentially determined by the density of nanoclusters within the FAs, as similar EED-NN distributions were obtained from simulations of particles uniformly distributed inside the experimentally obtained FAs, using identical particle densities as to the ones obtained experimentally for the integrin nanoclusters and the different adaptors (Materials & Methods) (Fig. 2D, black lines). Considering the canonical view that integrins inside FAs are bound to paxillin and engaged to talin and vinculin (43, 45), these results might be surprising at first sight, as one would expect a much higher fraction of EED-NN values

245 below zero. Nevertheless, using different super-resolution microscopy techniques, others have also found negligible spatial colocalization of integrins with these adaptor proteins (36, 37). Moreover, Dunn and co-workers also found that most ligand-bound integrins inside FAs exist in a minimally tensioned state (< 2 pN) and not dependent on the actin cytoskeleton (39). The results from the Dunn lab are fully in line with the lack of colocalization of integrins to talin
250 and vinculin as we determined here, since these two adaptors mediate the linkage of integrins to the actin cytoskeleton (43, 46). Nevertheless, we would like to mention that we labeled talin at its actin-binding C-terminal region, which in a 2D projection can appear to be at a distance of 100 nm or more from the N-terminal integrin-binding site (47), so lack of spatial overlap does not necessarily indicate lack of direct engagement.

255 It has been recently proposed that adhesion proteins including integrins organize in a hierarchical fashion inside FAs, forming nanoclusters similar to the ones reported here, that further enrich into compartmentalized regions around 300 nm in size (37). To enquire whether such hierarchical organization is present in our data, we performed nearest-neighbor distance (NND) analysis between nanoclusters of the same proteins (Fig. 2E). In addition, we
260 implemented simulations of uniformly distributed particles inside the experimental FA regions, using the same experimental nanoclusters densities, and made the corresponding NND analysis (Fig. 2E). Notably, our results show that the global organization of all the adhesion protein nanoclusters investigated is highly uniform inside FAs, as the experimental NND distributions were indistinguishable from those of randomly distributed particles (Fig. 2E). In contrast to the
265 recent findings of the Kusumi lab (37), we did not observe any evidence of spatial enrichment of protein nanoclusters inside FAs. Instead, the observed characteristic separation between nanoclusters appears to be solely determined by their density inside FAs.

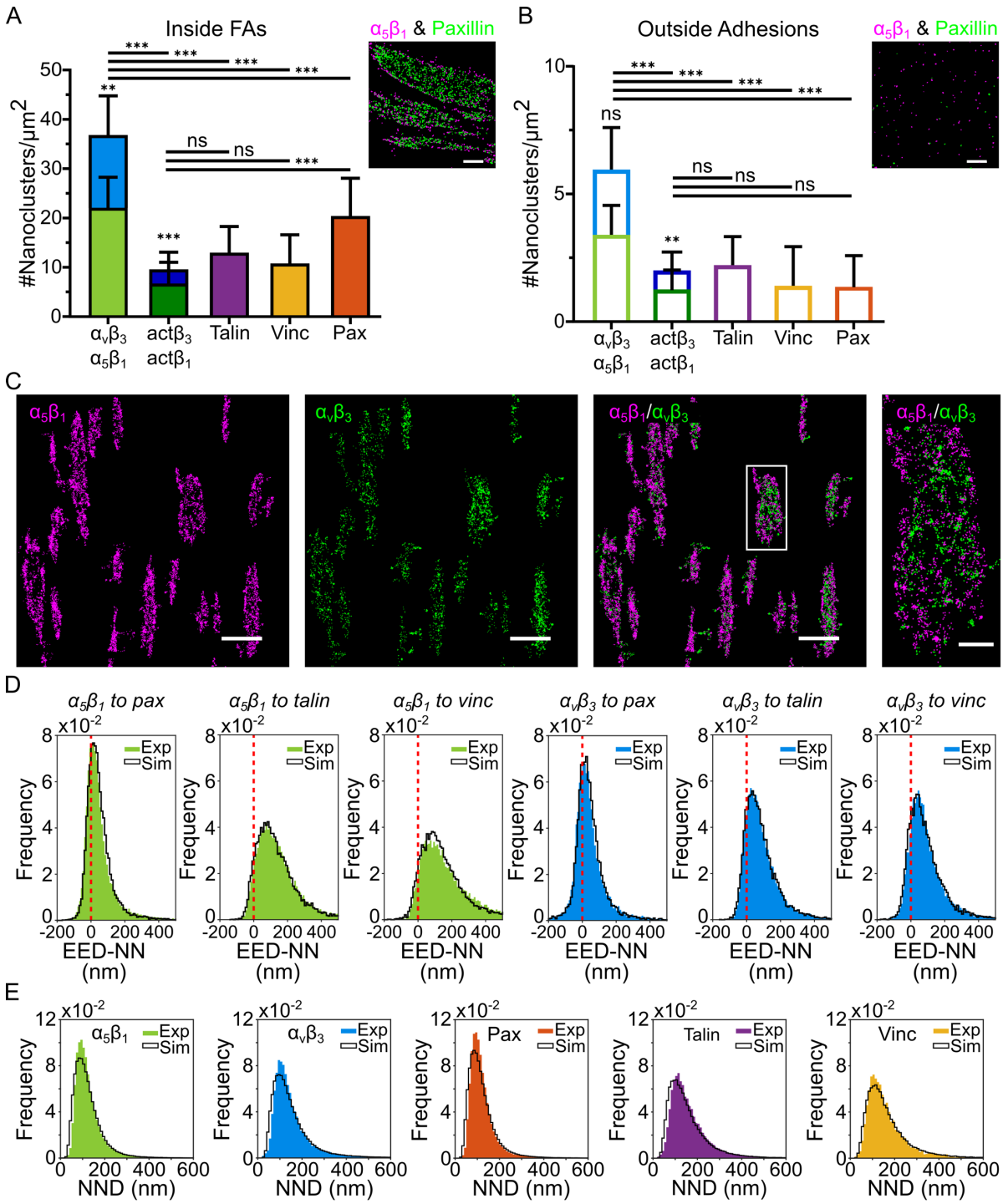

Figure 2 **Mesoscale organization of integrin nanoclusters and adaptor proteins inside FAs.** *(A, B) Mean density of nanoclusters per unit area inside FAs (A) and on the cell membrane outside adhesions (B), with $\alpha_5\beta_1$ and actβ_1 in light and dark green, respectively; and $\alpha_v\beta_3$ and actβ_3 in light and dark blue, respectively. The densities of integrins nanoclusters per unit area are shown as stacked graphs to allow comparison between the total number of integrin nanoclusters ($\alpha_5\beta_1$ and $\alpha_v\beta_3$) and the adaptor proteins. The bars show the mean ± st. dev of the distribution. Statistical significance between data of all proteins was tested using a multi comparison one-way ANOVA, assuming Gaussian distribution of points. The comparison between $\alpha_5\beta_1$ and $\alpha_v\beta_3$, (actβ_1 and actβ_3) was done with an unpaired t-test, where ns = not significant, $p>0.05$; *, $p<0.05$; **, $p<0.01$; ***, $p<0.001$. The insets show representative images of nanoclusters for $\alpha_5\beta_1$ (magenta) and paxillin (green) in FAs (A) and outside adhesions (B). Scale bar: 1 μm. (C) Representative dual-color STORM image of the total*

populations of $\alpha_5\beta_1$ (magenta) and $\alpha_v\beta_3$ (green) integrins inside FAs. The panel on the far-right side corresponds to a zoomed-in region of a single FA (white box) showing spatially segregated $\alpha_5\beta_1$ and $\alpha_v\beta_3$ nanoclusters. Scale bars: 2 µm, and 500 nm for the zoomed-in region. (D) Histogram of the EED-NN values between $\alpha_5\beta_1$ and the different adaptors (green) and, between $\alpha_v\beta_3$ and the adaptors (blue). The black line in each plot corresponds to the histogram for the simulated data sets. The dashed red line at zero corresponds to nanoclusters contiguous to each other. Percentage of overlapping nanoclusters: $\alpha_5\beta_1$-paxillin: exp = 28.4%, sim = 24.4%; $\alpha_5\beta_1$-talin: exp = 6.7%, sim = 8.1%; $\alpha_5\beta_1$-vinculin: exp = 6.0%, sim = 7.7%; $\alpha_v\beta_3$-paxillin: exp =31.7%, sim=29.2%; $\alpha_v\beta_3$-talin: exp =15.7%, sim=16.5; $\alpha_v\beta_3$-vinculin: exp =14.9%, sim=17.4%. (E) Histogram of the NND values between nanoclusters of the same protein. The black line in each plot corresponds to the histogram for the simulated data sets. Bin width is 10 nm.

Integrin $\alpha_5\beta_1$ but not $\alpha_v\beta_3$ nanoclusters are enriched on FA edges.

Our previous global analysis rendered a uniform inter-cluster organization of all adhesion protein nanoclusters inside FAs. Yet, visual inspection of the dual-color STORM images suggests that a significant fraction of $\alpha_5\beta_1$ nanoclusters preferentially localize on FA edges (Fig. 1B). To quantify these observations, we calculated the shortest-path distance from each $\alpha_5\beta_1$ nanocluster to the edge of its corresponding FA, i.e., its distance-to-FA-edge, and generated a histogram of these values (Fig. 3A). In addition, we generated a similar histogram from simulations of uniformly distributed $\alpha_5\beta_1$ nanoclusters on FAs (see Materials & Methods). In general, if the nanoclusters were uniformly distributed throughout the FA, one would expect that the probability of finding a nanocluster at a specific distance to the FA edge decreases with increasing distance. This occurs because there is a larger area along the perimeter of any given shape and thus a higher number of nanoclusters (e.g., for a circular shape, the decrease is linear with the distance to the FA edge). We found that our experimental and simulated data indeed exhibit this general trend, although, notably, a higher percentage of $\alpha_5\beta_1$ nanoclusters were detected at distances below 100 nm from the FA edges, as compared to a uniform distribution (Fig. 3A and *inset*), indicative of their preference to locate closer to the FA edges. Similar trends were also obtained for talin, and to a lesser extent for paxillin, whereas the distributions of $\alpha_v\beta_3$ and vinculin were indistinguishable from random (Fig. S4A).

To better assess the extent of nanocluster enrichment at FA edges at the single cell level, we computed the median values of the experimentally obtained distance-to-FA-edge distributions per cell (over multiple FAs) and those corresponding to the simulated data. We then defined the edge-proximity-factor (EPF) as the relative difference between experimental and simulated distributions, where negative EPF values correspond to preferential nanocluster enrichment at FA edges, positive EPF values to nanocluster depletion at FA edges, and EPF = 0 corresponds to random location of nanoclusters with respect to the FA edges (Fig. 3B). Moreover, to statistically determine whether the distribution of EPF values was different from zero (the EPF

value expected from a random distance-to-the-FA-edge distribution) we ran a paired Student's t-test for each protein comparing the experimental with the corresponding simulated distributions. This analysis showed that most proteins exhibit some degree of enrichment at the edges of the FAs (i.e., negative EPF values), although their magnitude was markedly different amongst them (Fig. 3B). The highest enrichments at the FA edges were found for the full population of $\alpha_5\beta_1$ nanoclusters and the active β_1 sub-population (~30% closer to the FA edge than if uniformly distributed) and for talin, whereas the enrichment at the FA edges of the total $\alpha_v\beta_3$ population and paxillin was much more modest. Notably, the active β_3 sub-population and vinculin showed no preferential enrichment at the FA edges (Fig. 3B).

To establish the characteristic distances at which nanocluster enrichment occurs with respect to the FA edges, we next computed the difference between the experimental and simulated distributions, i.e., the variation from random, as a function of the distance to the FA edges, for each of the examined proteins (Fig. 3C, D). Here, positive values correspond to local nanocluster enrichment at a given distance to the FA edge, whereas negative values indicate nanocluster depletion. Our results show a clear difference between both integrins, with $\alpha_5\beta_1$ nanoclusters being enriched close to the edge of FAs (Fig. 3C, continuous green line) whereas $\alpha_v\beta_3$ nanoclusters showed a rather uniform distribution, regardless of their distance to the FA edges (Fig. 3C, continuous blue line). Moreover, the preferential enrichment of β_1 but not of β_3 nanoclusters at the FA edges was retained when specifically analyzing the active integrin conformations (Fig. 3C, dashed green and blue lines, respectively).

We next investigated how adaptor protein nanoclusters distribute with respect to the FA edge using a similar approach. We found that both talin and paxillin nanoclusters showed enrichment in a region between 50–150 nm from the FA edges, although somewhat less pronounced as compared to $\alpha_5\beta_1$ nanoclusters (Fig. 3D), whereas vinculin nanoclusters showed no preference to reside proximal to the FA edges. Finally, we extracted the percentage of the total $\alpha_5\beta_1$ and active β_1 nanoclusters that reside within distances shorter than 100 nm from the FA edges and compared the results to those from simulations of random organization (Fig. 3E). Notably, a significantly larger percentage of active β_1 nanoclusters as compared to the total $\alpha_5\beta_1$ nanocluster population and to the simulations, locate at the periphery of FAs (Fig. 3E).

Together, these results strongly indicate that integrin nanoclusters spatially organize in a rather distinct fashion within FAs, with $\alpha_5\beta_1$ nanoclusters localizing preferentially at the edges of the FAs and $\alpha_v\beta_3$ nanoclusters distributing randomly inside FAs. Moreover, the preferential enrichment of active β_1 nanoclusters together with talin at the FA edges suggests that β_1 activation is spatially regulated inside FAs.

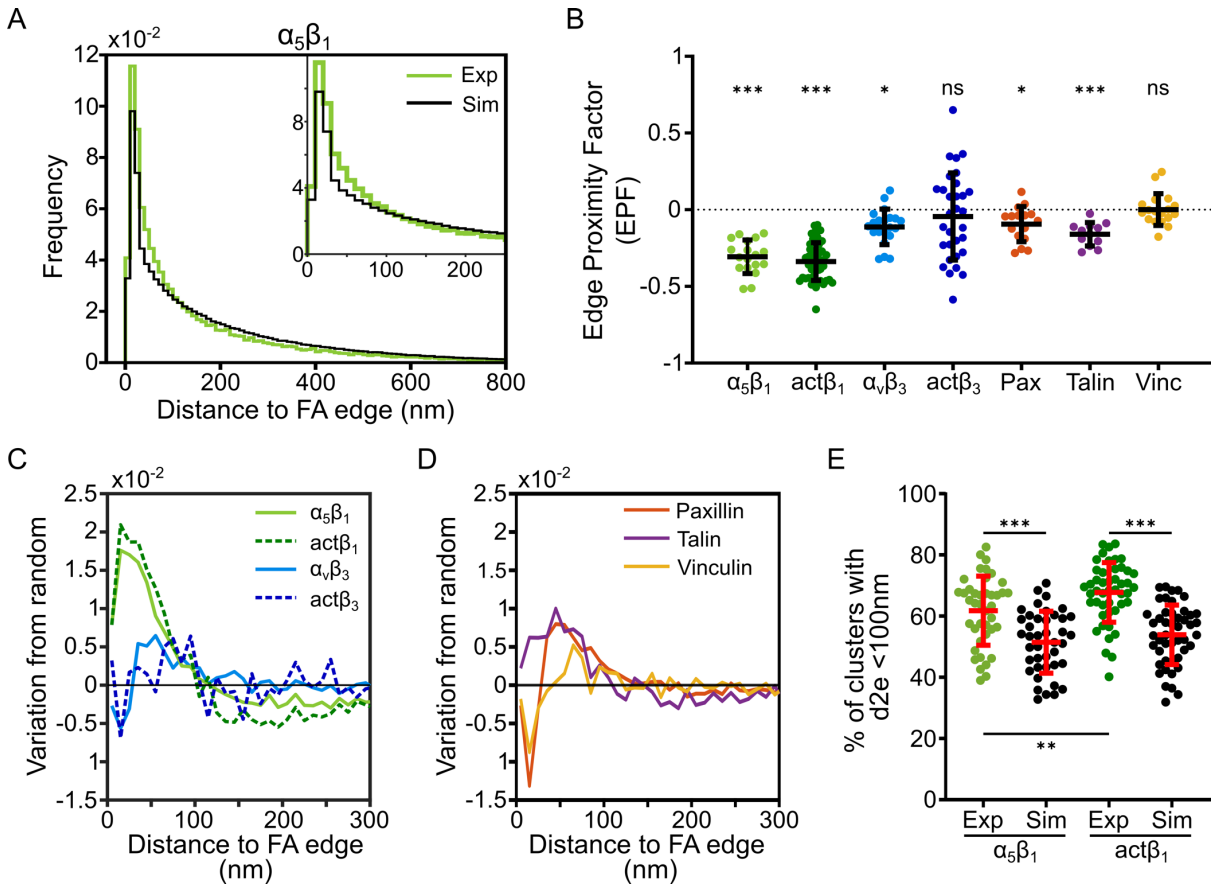

Figure 3 **Integrin $\alpha_5\beta_1$ nanoclusters are preferentially distributed on the edges of FAs.** *(A) Distribution of distances from the center of mass (CoM) position of each individual $\alpha_5\beta_1$ nanocluster to its closest FA edge obtained from DBSCAN-analyzed STORM images. The histogram represents the frequency distribution over all cells. Green lines correspond to the experimental data (Exp) and the simulated uniform distribution (Sim) is shown as a black histogram. Bin width is 10 nm. The inset shows the distribution for the first 250 nm. (B) Edge Proximity Factor (EPF) per cell for each of the proteins investigated. Data are shown as median values per individual cell (color dots). The mean ± st. dev. over all the cells are superimposed as black lines. Statistical significance between experimental and simulated data was tested using a paired t-test, where ns = not significant, p>0.05; *, p<0.05; **, p<0.01; ***, p<0.001. (C, D) Variation of the nanocluster distances from the FA edges with respect to random organization, as function of the distance to the FA edges for $\alpha_5\beta_1$ and $\alpha_v\beta_3$ integrin nanoclusters (C) and for the adaptor proteins (D). (E) Percentage of nanoclusters proximal to FA edges (<100nm) for the total and active β_1 nanocluster population (color dots) together with results from simulations of random organization (black dots). Each dot corresponds to the median value per cell, each cell containing multiple FAs. The mean ± st. dev. over all the cells is superimposed as red lines. Statistical significance between experimental and simulated data was tested using a paired t-test, and to test the significance between $\alpha_5\beta_1$ and actβ_1 the unpaired t-test was used, assuming a Gaussian distribution of data, where ns = not significant, p>0.05; *, p<0.05; **, p<0.01; ***, p<0.001.*

Active β_1 nanoclusters form multiprotein hubs at FA edges.

Since activation of integrins involves engagement with their adaptors paxillin, talin and vinculin, we sought to investigate whether the active β_1 nanoclusters preferentially located at the FAs periphery also reside in proximity to their adaptor proteins. For this we first obtained the inter-nanocluster NND (*i*NND) distributions between active β_1 nanoclusters and each of the adaptor nanoclusters (Fig. S4B). We calculated the median of each *i*NND distribution and used this value as a threshold to classify pairs of active β_1-adaptor nanoclusters as being close (i.e., *i*NND < median) or far (*i*NND > median) from each other. Next, we separately computed the distance-to-the-FA edge for the active β_1 nanoclusters that were found close or far from their partner and compared the results to simulated data (Fig. 4A and *inset*). Having these plots, we then calculated the variation from random (i.e., difference between experimental data and simulations of random organization) as a function of the distance to the FA edge, for both active β_1 nanoclusters close to their partner and active β_1 nanoclusters far from their partner (Fig. 4B and Fig. S4C). This analysis shows that active β_1 nanoclusters preferentially locate the FA edges regardless of their proximity to talin nanoclusters (Fig. 4B) and to other adaptors (Fig. S4C). In contrast, the same analysis on active β_3 nanoclusters shows a random distribution inside of FAs irrespective of their proximity to talin or other adaptor nanoclusters (Fig. 4C).

Finally, we enquired whether adaptor protein nanoclusters (paxillin, talin, and vinculin) close to active β_1 nanoclusters also locate closer to the FA edges. Notably, we found that all of these adaptor nanoclusters close to active β_1 nanoclusters are also enriched on the FA edge region (~150–200 nm from the edge), whereas adaptor nanoclusters far from active β_1 appear to be more uniformly distributed (Fig. 4D–F). Taken together, our data reveal a differential mesoscale organization between active β_1 and β_3 nanoclusters inside FAs, with active β_1 nanoclusters being enriched at the periphery of FAs alongside adhesion adaptor nanoclusters, while active β_3 nanoclusters remain uniformly distributed throughout FAs, lacking peripheral enrichment.

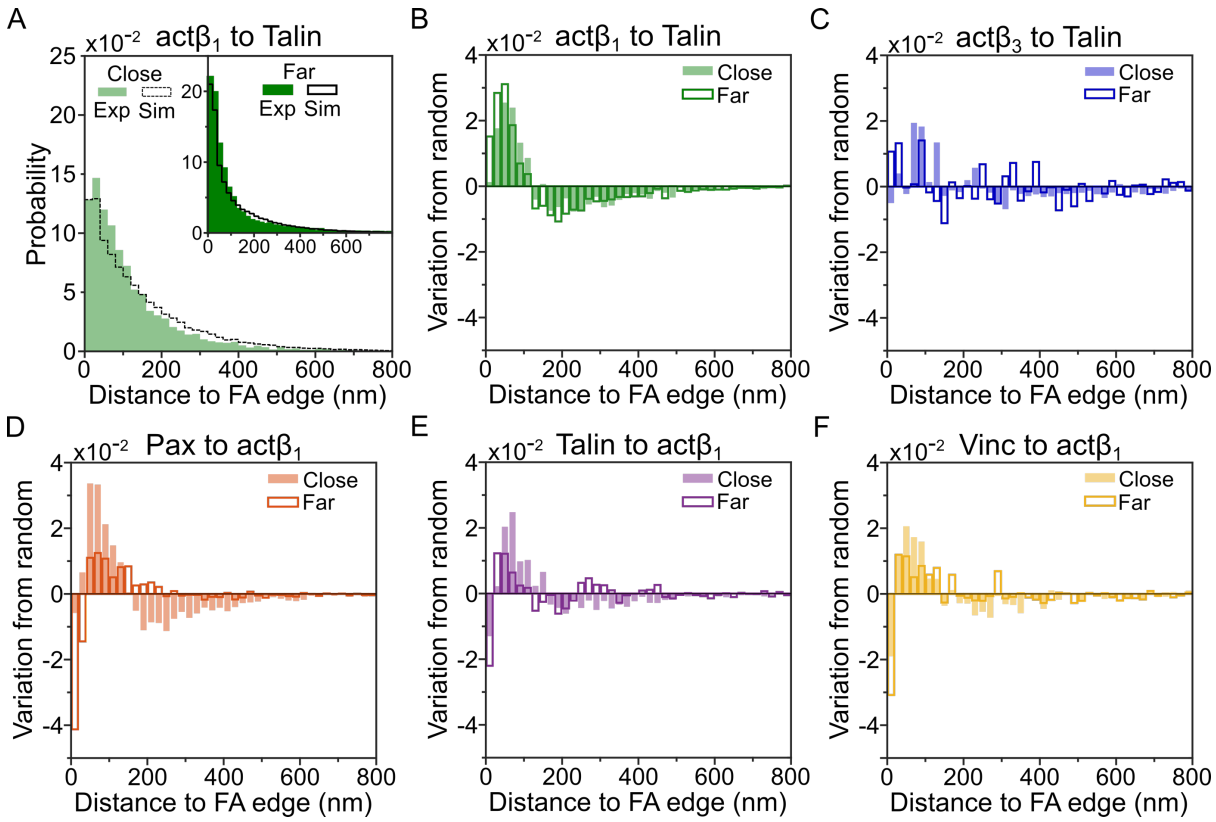

Figure 4 **Active β_1 nanoclusters form multiprotein hubs at the FA edges.**
(A) Population of active β_1-talin nanocluster pairs as a function of their distance-to-the-FA edge. The data plotted in light green correspond to active β_1 nanoclusters located close to talin (i.e., iNND < median), while the inset dark green corresponds to active β_1 nanoclusters located far from talin (i.e., iNND > median). iNND distributions are shown in Fig. S4B. Black lines are for simulated data sets. Bin width is 20 nm. (B) Variation from random for active β_1-talin nanocluster pairs as function of their distance-to-the-FA-edge. Filled bars correspond to active β_1 nanoclusters located close to talin (iNND < median) and empty bars correspond to active β_1 nanoclusters located far from talin (iNND > median) (C) Similar to (B) but for active β_3 nanoclusters. (D-F) Variation from random for paxillin (D), talin (E), vinculin (F) active β_1 nanocluster pairs, as function of their distance-to-the-FA-edge, with data segregated in two different distributions according to the pairs proximity. Bin width is 20 nm.

Discussion

Here, we have combined dual-color super-resolution optical microscopy together with a robust set of analytical tools to provide insights on the lateral spatial organization of different adhesion proteins inside FAs. Earlier reports showed that nascent adhesions (NAs) are formed due to integrin nanoclusters that either rapidly disassemble at the plasma membrane without force or further mature into FAs in response to mechanical forces (35, 48). Our results now show that even in the presence of mechanical forces (i.e., inside FAs), integrin nanoclusters remain segregated from each other while maintaining their sizes and number of molecules. Similar integrin nanocluster properties were also found outside adhesions, reinforcing the notion that integrin nanoclustering is force-independent (35). Interestingly, we found that the main cytoplasmic adaptors, paxillin, talin and vinculin, also form nanoclusters of similar size and

420 number of single molecule localizations as the integrins, regardless of whether they locate inside or outside FAs. The presence of adhesion protein nanoclusters outside of FAs is intriguing. However, immobilized (active) integrins have been previously observed outside of FAs (25, 49). We suggest that these isolated nanoclusters may represent transient nascent adhesions forming on the cell membrane. Although STORM images do not allow to directly
425 extract the actual number of proteins contained in nanoclusters given the primary and secondary antibody labeling strategy used, the similarity in terms of number of single molecule localizations amongst integrins and their adaptor partners suggest that these nanoclusters might be stoichiometrically similar. Together, our results strongly indicate that adhesion proteins organize as universal nano-hubs, functioning as modular adhesion units to serve multiple
430 integrin-dependent functions related to adhesion and migration but also to mechanosensing and mechanotransduction.

Consistent with previous results (36), our data revealed that active and inactive $\alpha_5\beta_1$ nanoclusters coexist inside FAs but are fully segregated from each other. Remarkably, $\alpha_v\beta_3$ also exhibits similar nanoscale segregation, with total population-to-active integrin ratios
435 indicating a similar segregation between active and inactive β_3. Furthermore, earlier data from our group demonstrated that the integrin $\alpha_L\beta_2$ expressed on leukocytes also segregates into active and inactive nanoclusters (50, 51). Thus, lateral segregation between active and inactive integrin nanoclusters may represent a common feature to spatially coordinate integrin activation. How could such cooperativity in integrin nanocluster activation arise? Our data
440 show a nearly 1:1 stoichiometry in the number of active integrin nanoclusters, and the main cytoplasmic adaptors talin and vinculin, known to activate integrins by their engagement to the actin cytoskeleton. The availability of a similar number of adaptor nanoclusters containing comparable number of molecules as the integrin nanoclusters suggests that inactive integrin nanoclusters are poised for their collective nanocluster activation, which is achieved upon the
445 concurrent engagement of talin and vinculin nanoclusters (and most probably also paxillin). This mechanism has been shown to operate in NAs in which concurrent recruitment of talin and vinculin prior to force generation is required for integrin activation and further maturation of NAs (52). In addition, our data reveals that there is a large percentage of inactive $\alpha_5\beta_1$ and $\alpha_v\beta_3$ integrins inside FAs and very little spatial overlap between integrins and main adaptors.
450 As integrin activation is highly dynamic and transient, we propose that this pool of inactive integrin nanoclusters is required to increase the probability of new engagements between integrins and their adaptors once the active integrin nanoclusters become disengaged,

stabilizing as a whole the FAs for lifetimes much longer than the binding-unbinding dwell-times of integrins with their partners.

Quantification of super-resolution data showed a higher number of $\alpha_5\beta_1$ nanoclusters compared to their $\alpha_v\beta_3$ counterparts inside FAs. The relative percentage of active β_1 nanoclusters is also higher than that of $\alpha_v\beta_3$ and moreover these two integrin nanoclusters never intermix inside FAs. Importantly, active β_1 nanoclusters preferentially locate at the periphery of FAs and in proximity with paxillin, talin and vinculin nanoclusters, while active β_3 are more uniformly distributed inside FAs. The differential degree of $\alpha_5\beta_1$ and $\alpha_v\beta_3$ in terms of expression, activation state, and lateral nano- and meso-scale segregation, strongly indicates that integrin activation and their distinct functions inside FAs are spatially regulated (Fig. 5). Based on our results we postulate that *(i)* $\alpha_5\beta_1$, through the ring on the FA periphery and its close proximity to paxillin, talin and vinculin nanoclusters, primarily functions for substrate attachment in its high tensional state, engaging with actomyosin filaments; *(ii)* $\alpha_v\beta_3$ and $\alpha_5\beta_1$ integrin nanoclusters in the central region of the FA undertake the role of mechanotransduction, being more dynamic in terms of activation and inactivation states and most probably engaged with shorter branched actin filaments; and *(iii)* the difference in these roles is controlled by the distinct mechanical forces exerted on the integrins, depending on their location inside FAs, and for $\alpha_5\beta_1$ perhaps also on its different tensional states (53).

Intriguingly, our analysis showed that active β_1 nanoclusters preferentially locate the FA edges regardless of their proximity to talin nanoclusters (Fig. 4B). These data are striking since active integrins are expected to be bound to both its ligand and talin, and therefore had anticipated the whole active β_1 population to be in close proximity to talin nanoclusters. We can envisage two plausible explanations for active β_1 to be far from talin. One possible scenario is the existence of other adaptor protein(s), aside from talin, able to bind to active β_1. Such a candidate might be tensin3, which has been recently shown to compete with talin to bind $\alpha_5\beta_1$, during the formation of fAs from FAs (54) A second possibility to explain our observations is the nature of talin itself. As a long rod-like protein, talin stretching experiments have shown that the N- and C- termini can be separated up to 250 nm due to actomyosin activity (55). Since we detect talin by labeling it in its C-terminal domain, which is opposite to the integrin binding side, it is possible that active β_1 is engaged to extended talin even for inter-cluster distances larger than the median *i*NND. Further experiments using specific antibodies against tensin3 as well as labeling talin at the closest proximity to the integrin binding side would clarify the adaptor partners associated to active β_1 nanoclusters at the periphery of FAs.

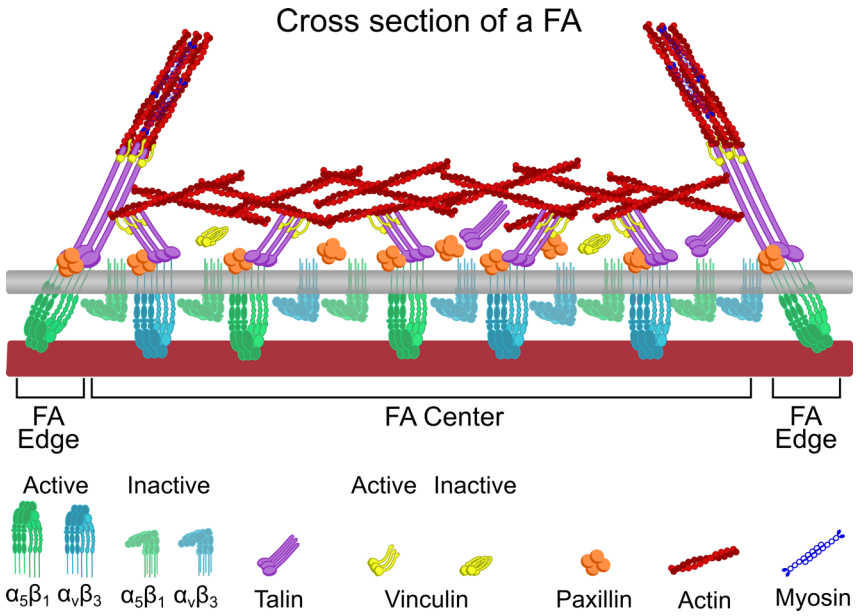

Figure 5 **Spatial regulation and activation of integrin nanoclusters and protein adaptors inside focal adhesions.**

$\alpha_5\beta_1$, $\alpha_v\beta_3$, and main protein adaptors organize as small nanoclusters inside FAs physically segregated from each other. A considerable high fraction of $\alpha_5\beta_1$ and $\alpha_v\beta_3$ integrins remain in an inactive state and do not intermix at the nanoscale. Active β_1 nanoclusters (green) on the FA edge reside in close proximity to the adaptor protein nanoclusters and thus possibly engaged to actomyosin filaments (red and blue). Integrin nanoclusters in the FA center are more randomly distributed with respect to one another, most probably engaged with branched cortical actin. According to our results we propose that $\alpha_5\beta_1$ nanoclusters located at the FA periphery could be primarily involved in cell substrate attachment, whereas $\alpha_5\beta_1$ and $\alpha_v\beta_3$ nanoclusters at the center of FAs engage in mechanosensing and mechanotransduction. For simplification, we show a cross-section of a FA where active β_1 integrins at the edge are engaged with talin. However, our data also show the presence of active β_1 nanoclusters spatially separated from talin and thus possibly engaged to other binding partners linking β_1 to the actin cytoskeleton (not shown in the cartoon for the sake of clarity).

In summary, in contrast to the classical textbook view where FAs are pictured as dense and homogenous assemblies of integrins fully engaged to their cytoplasmic adaptors, our work reveals a highly complex organization inside FAs, where regulation of different integrins and their activation state are highly coordinated in space. We believe that such spatial regulation provides the means for different integrins to synergize and/or diversify their functions in terms of adhesion, migration, mechanosensing and mechanotransduction. Earlier reports showed that proteins such as KANK1, KANK2, and β_1 integrins are enriched at the edges of adhesions, with KANK2 reducing the force exerted by the cells through its binding to talin (56, 57). KANK proteins have also been implicated in enabling communication between microtubules and actin by binding to talin and liprin-β_1 at FA edges (58). More recent data suggest that the localization of KANK1 around FAs is driven by liquid-liquid phase separation (59). Our findings together with those mentioned above suggest that the $\alpha_5\beta_1$ nanocluster belt is an important feature of FAs and may be critical for their function. However, further research is needed to fully

understand how the organization of these key proteins contributes to their roles FAs. p130Cas-
515 and FAK-dependent phase separation has been also suggested to promote integrin clustering and NA assembly (60). Whether phase separation also contributes to the preferential organization and activation of β_1 at the FA edges as we reveal here is an intriguing topic that deserves further investigation.

Materials and Methods

520

Sample preparation and immunolabeling. HFF-1 cells (human foreskin fibroblasts) were obtained from ATCC and used with low passage number (passage <15). Cells were maintained in DMEM supplemented with 15% FBS and cultured in a humidified atmosphere at 37º C and 5% CO_2. Experiments were performed in cells seeded on 8-well plates (#1 Lab-Tek,
525 Thermofisher, #155411) that were previously coated with fibronectin (FN) at full substrate coverage. FN coating was performed by incubation with 10 µg/ml FN for 30 min at room temperature (RT). We note that FBS can contain vitronectin (VN) and other proteins that may act as ligands of integrins. However, since the glass slides are saturated with FN prior to incubation with cells and media, FN remains the dominant ligand in our experiments. After
530 seeding, cells were allowed to spread for 24 h at 37º C and 5% CO_2, after which they were fixed by using 4% PFA in PBS for 15 min at RT. Cells were permeabilized using 0.1% Triton X-100 in PBS for 10 min and blocked with 3% BSA in PBS for 40 min. Primary antibodies against integrins $\alpha_5\beta_1$ and $\alpha_v\beta_3$, total population, or specific for the active conformation of integrins β_1 and β_3, and total populations of adaptor proteins, paxillin, talin (actin binding C-
535 terminal epitope), or vinculin, were diluted in blocking buffer and added to the cells for 30 min at RT. After washing with PBS, secondary antibodies that were conjugated in-house with dye pairs Alexa Fluor 405-Alexa Fluor 647 (405-647 channel) or Cy3B-Alexa Fluor 647 (Cy3-647 channel), were added to the cells for 30 min at RT (see Tables S1-S3 for details on reagents and antibodies used). After washing with PBS, cells were stored in PBS until imaged.

540 **Image acquisition.** STORM data were obtained on a commercial Nikon Eclipse Ti system (N-STORM), equipped with a 100x oil objective with NA 1.49 using TIRF illumination. The detector was an ANDOR technology EMCCD iXon 897 camera, with a 256x256 pixel ROI and a pixel size of 160 nm. The system has an Agilent technologies laser box with wavelengths of 405 nm, 560 nm and 647 nm. STORM was performed by incubating cells in an imaging
545 buffer containing 100 mM of the reducing agent cysteamine mercaptoethylamine (MEA) (77 mg of MEA in 1 ml of 360 mM HCl, stock solution 1 M), the enzymatic oxygen scavenger Glox solution (0.5 mg/ml glucose oxidase, 40 µg/ml catalase), and 6.25% glucose in PBS.

Details of the STORM imaging buffer reagents are found in Table S4. Dual color imaging was carried out cyclically and sequentially. In brief, we first detected the 405-647 channel in a 5-
550 frame cycle consisting of 1 activator frame (405 nm laser on) followed by 4 reporter frames (647 nm laser on), followed by the Cy3-647 channel detection sequence, similarly composed of 1 activator frame (560 nm laser on) followed by 4 reporter frames (647 nm laser on). The frame rate was 50 Hz (20 ms per frame) for all frames. Imaging was carried out by cyclically repeating this 10-frame sequence until all the reporter dyes were exhausted (typically ~70,000
555 frames).

Single molecule detection, localization precision, and STORM image reconstruction. Dual-color STORM image reconstruction was done using Insight3 software, provided by Bo Huang (UCSF, initially developed in Xiaowei Zhuang's lab, Harvard University). In each imaging frame, individual molecules were identified using intensity thresholding (gray levels
560 set between 600-60,000), then each intensity profile was fitted with a 2D Gaussian function to identify the central position, i.e., the coordinates that represent the spatial localization of that fluorescent molecule. The analysis was run over the entirety of each data set, resulting in a final output that is a list of x,y coordinates (localizations) corresponding to each individual molecule that has been identified. Insight3 software allows for drift correction using the correlated
565 function of the image, for details see (61). In this multi-color imaging scheme, the main source of crosstalk is the nonspecific activation of the Alexa 647 by the 647 nm laser (62), which is activator-independent and can occur in any frame. We implemented statistical crosstalk correction where the Insight3 software analyses the full image in 50x50 nm regions of interest (ROIs) and determines if each ROI is predominantly one color of the other. Based on the
570 acquisition design (in our case, one activator frame followed by four reporter frames) the software determines the probability of detecting a nonspecific reporter molecule (62). To minimize color cross-talk, only those localizations detected in the second frame of each five-frame STORM imaging cycle (that is, the first of the four reporter frames) were considered for future analytical steps. Since each single molecule can experience numerous blinking events,
575 the variation of the x,y coordinates from frame to frame determines the effective resolution (63). To measure this, we detected multiple localization events arising from individual molecules deposited on glass and calculated the standard deviation of the localization positions. We measured the effective resolution of our system to be ~15 nm. These localizations detected from nonspecific antibodies on glass were also used to set a threshold for what we considered
580 to be a nanocluster of proteins. We found that the antibodies on glass had a median number of

localizations of 5 (for channel 1) and 3 (for channel 2). With the aim of discarding all localizations coming from nonspecific binding or binding to individual proteins we set the threshold at 10 localizations per nanocluster.

Generation of masks and classification of the localizations belonging to FAs, fAs or outside adhesions. A Fiji plugin, developed by the Lakadamyali lab, was implemented as an initial step to split the localization data from the STORM images into separate data sets corresponding to the localizations contained in certain ROIs (64). First, the data from the two channels of the reconstructed STORM image were imported and the localizations rendered together in a 1024x1024 pixels image (Fig. S1A). Next, we applied an intensity threshold, until the adhesion areas were visually detected, a Gaussian blur of the image (by 2 pixels), and a second threshold filter until a smooth binary mask was obtained (Fig. S1B). The final mask retaining only the adhesion areas was obtained by manually selecting the regions corresponding to the adhesion complexes (identified by visual inspection based on their size and location). In the first steps, this Fiji plugin creates separate files containing the localizations that fall within the selected ROIs: all adhesions, glass, and outside adhesions (i.e., cell membrane that contain the remaining areas of the image that do not correspond to all adhesions or glass). In a second step the "all adhesions" file was again analyzed by the same plugin and all adhesions were split into FAs and fAs and rendered with Insight3. Fig. S1C-F shows the resulting rendered localizations for the different regions. These final two-color files for different cell regions were then individually and independently analyzed.

Image analysis. *Clustering detection using the DBSCAN algorithm.* DBSCAN is a density-based data clustering algorithm designed to be executed on arbitrary data sets with minimal input from the user (40). The algorithm works by identifying arbitrary-shaped clusters of data points using two user-defined input values: epsilon (ε), which is a radial distance that serves to define a local neighborhood from a randomly selected initial data point; and N_{min}, which is the minimum number of points required to be within the initial point's neighborhood, so it is considered part of the cluster seed. For our image analysis, spots on glass outside the cell regions were analyzed using $\varepsilon = 20$ nm and $N_{min} = 2$, in order to define a minimum threshold for the number of localizations per nanocluster. Important to note that we carried out this analysis on glass areas, next to the cells, found in all of our STORM images. In this way we ensure having the same imaging conditions for in-cell nanoclusters and for spots-on-glass, however, at the expense of having a broader distribution of localization per spot-on-glass due to the presence of cell debris on the glass. When analyzing the nanoclusters found in ROIs

within the cell, the DBSCAN parameters were set to ε = 20 nm and N_{min}=3 localizations, which
615 are common values used in the field (36, 41). Nevertheless, since multiple blinks of a fluorophore might result in artifactual clusters, we only considered true nanoclusters as those containing 10 or more localizations. Examples on the identification of different nanoclusters by DBSCAN are shown in Fig. S1G. The algorithm also provides the center of mass (CoM) coordinates of each nanocluster together with the number of localizations per nanocluster and
620 their diameter.

Nearest neighbor distance (NND) analysis. To establish how the protein nanoclusters are distributed relative to one another, we used the MATLAB (MathWorks) function *knnsearch*. This function computes for each nanocluster the NND, which is the shortest distance from the CoM of a given nanocluster to its closest CoM nanocluster neighbor. We also used the same
625 function to determine the *i*NND (i.e., NND between nanoclusters of different proteins). To measure the percentage of nanoclusters that overlap (colocalization fraction), we first computed the edge-to-edge distance between nearest neighbors (EED-NN) by subtracting from the NND the radii of the two-corresponding near-neighbor nanoclusters. From the EED-NN distributions we calculated the percentage of occurrences with EED-NN values below zero.
630 The *knnsearch* function was also used to extract the distance-to-the-FA edge, i.e., the shortest distance between nanoclusters and the edge of adhesions. To that end, we computed the NND between the CoM of each nanocluster to the center coordinates of the list of pixels that fall on the edge of the FA mask.

Computational generation of uniform nanocluster distributions. To assess whether the
635 distance distributions obtained from the experimental data (NND, EED-NN and distance-to-the-FA-edge), correspond to a preferential type of organization or to a uniform distribution, we performed simulations by generating in silico histograms of non-overlapping and randomly distributed nanoclusters inside FAs. For this, we first extracted the exact number and size of nanoclusters per adhesion from the experimental data. Although our initial approach was to
640 computationally generate the same number of nanoclusters and distribute them uniformly over the adhesion masks regardless of their physical size, we found that this approach was not computationally suitable. The reason for it is that in many cases the large nanoclusters did not fit (without overlapping) in the remaining space available within the adhesions after randomly positioning the large majority of smaller nanoclusters. We thus opted for classifying the
645 nanoclusters according to their physical size and then start our procedure by first positioning the largest nanoclusters and later all the remaining smaller ones. In addition, as our

experimental data renders well segregated nanoclusters, we imposed in our algorithm the condition that nanoclusters should not overlap with one another. Fig. S5 shows the different steps followed in order to generate distributions of random nanoclusters inside FAs.

Statistical analysis. Statistical analysis was carried out using GraphPad Prism (version 9.12). The details of the individual statistical tests as well as the level of significance along with p-values are explicitly provided in the figure legends. No predetermined statistical method was employed for establishing the sample size, as the sample sizes were not selected based on a predefined effect size. In this context, multiple experiments were independently performed, employing various sample replicates, as detailed in Table S5.

Supplemental material

The supplemental material contains five different Tables that specify the reagents used for cell culture and sample preparation, the primary antibodies used in the experiments, the secondary antibodies and their fluorophores used in STORM experiments, a list of the reagents and dyes used for STORM imaging, and finally, a summary of experiments analyzed either as individual proteins or in protein pairs. In addition, the supplementary material contains five different supplementary figures together with their captions. Fig. S1 provides information on the analysis pipeline used to identify and characterize nanoclusters of the different proteins. Fig. S2 provides quantification of the nanocluster sizes and number of localizations inside FAs and outside ACs for all the proteins investigated. Fig. S3 provides quantification of the edge-to-edge distance for the protein nanocluster pairs investigated and percentage of nanoclusters that physically overlap with each other. Fig. S4 provides quantification of how different protein nanoclusters are organized with respect to the FA edge as well as quantification of *i*NND distributions between active β_1 nanoclusters and their adaptor partners paxillin, talin and vinculin. Fig. S5 illustrates the different steps followed to generate in-silico distributions of non-overlapping, randomly distributed nanoclusters inside FAs.

Data Availability Statement

The data supporting the findings of this study are available from the corresponding author upon reasonable request. The codes used in this study are available from the corresponding author upon reasonable request.

Acknowledgments

The authors would like to thank J. Andilla and M. Rivas for technical support and to the Lakadamyali lab for the Fiji plugin used to split data into ROIs. The research leading to these

results has received funding from the European Commission H2020 Program under grant agreement ERC Adv788546 (NANO-MEMEC) (to M.F.G.-P.), Government of Spain (Severo Ochoa CEX2019-000910-S, State Research Agency (AEI) (PID2020-113068RB-I00 / 10.13039/501100011033 (to M.F.G.-P.), RYC-2017-22227 and PID2022-138282NB-I00 project funded by the MCIN/AEI/10.13039/501100011033/ FEDER, UE (to F.C.)), Fundació CELLEX (Barcelona), Fundació Mir-Puig and the Generalitat de Catalunya through the CERCA program and AGAUR (Grant No. 2021 SGR01450 M.F.G.-P.). N.M. acknowledges funding from the European Union H2020 under the Marie Sklodowska-Curie grant 754558-PREBIST. The authors declare no competing financial interests.

Author Contributions: S.K prepared the biological samples, performed STORM imaging and analyzed the data. N.M. developed algorithms for data analysis and contributed to the analysis. F.C. and M.F.G.-P. supervised the research. S.K., F.C. and M.F.G.-P conceived and discussed the experiments, interpreted the data, and wrote the paper.

References

1. B. Geiger, J. P. Spatz, A. D. Bershadsky, Environmental sensing through focal adhesions. *Nat Rev Mol Cell Biol* **10**, 21–33 (2009).
2. M. K. L. Han, J. De Rooij, Converging and Unique Mechanisms of Mechanotransduction at Adhesion Sites. *Trends Cell Biol* **26**, 612–623 (2016).
3. J. D. Humphrey, E. R. Dufresne, M. A. Schwartz, Mechanotransduction and extracellular matrix homeostasis. *Nat Rev Mol Cell Biol* **15**, 802–812 (2014).
4. K. A. Jansen, P. Atherton, C. Ballestrem, Mechanotransduction at the cell-matrix interface. *Semin Cell Dev Biol* **71**, 75–83 (2017).
5. P. Roca-Cusachs, N. C. Gauthier, A. Del Rio, M. P. Sheetz, Clustering of α5β1 integrins determines adhesion strength whereas αvβ3 and talin enable mechanotransduction. *Proc Natl Acad Sci U S A* **106**, 16245–16250 (2009).
6. A. Elosegui-Artola, *et al.*, Mechanical regulation of a molecular clutch defines force transmission and transduction in response to matrix rigidity. *Nat Cell Biol* **18**, 540–548 (2016).
7. C. T. Mierke, Bidirectional Mechanical Response Between Cells and Their Microenvironment. *Front Phys* **9**, 1–40 (2021).
8. N. D. Gallant, K. E. Michael, A. J. García, Cell Adhesion Strengthening: Contributions of Adhesive Area, Integrin Binding, and Focal Adhesion Assembly. *Mol Biol Cell* **16**, 4329–4340 (2005).
9. J. D. Humphries, *et al.*, Vinculin controls focal adhesion formation by direct interactions with talin and actin. *Journal of Cell Biology* **179**, 1043–1057 (2007).
10. A. Elosegui-Artola, *et al.*, Rigidity sensing and adaptation through regulation of integrin types. *Nat Mater* **13**, 631–637 (2014).
11. N. Strohmeyer, M. Bharadwaj, M. Costell, R. Fässler, D. J. Müller, Fibronectin-bound α5β1 integrins sense load and signal to reinforce adhesion in less than a second. *Nat Mater* **16**, 1262–1270 (2017).
12. Y. L. Hu, *et al.*, FAK and paxillin dynamics at focal adhesions in the protrusions of migrating cells. *Sci Rep* **4**, 1–7 (2014).

13. C. Egles, *et al.*, Integrin-Blocking antibodies delay Keratinocyte Re-Epithelialization in a Human three-dimensional wound healing model. *PLoS One* **5**, 2–9 (2010).

14. G. Neiman, *et al.*, Integrin alpha-5 subunit is critical for the early stages of human pluripotent stem cell cardiac differentiation. *Sci Rep* **9**, 1–10 (2019).

15. J. L. Walker, R. K. Assoian, Integrin-dependent signal transduction regulating cyclin D1 expression and G1 phase cell cycle progression. *Cancer and Metastasis Reviews* **24**, 383–393 (2005).

16. R. Pytela, M. D. Pierschbacher, E. Ruoslahti, Identification and isolation of a 140 kd cell surface glycoprotein with properties expected of a fibronectin receptor. *Cell* **40**, 191–198 (1985).

17. I. F. Charo, L. Nannizzi, J. W. Smith, D. A. Cheresh, The vitronectin receptor α(v)β3 bind fibronectin and acts in concert with α5β1 in promoting cellular attachment and spreading on fibronectin. *Journal of Cell Biology* **111**, 2795–2800 (1990).

18. E. Ruoslahti, RGD and other recognition sequences for integrins. *Annu Rev Cell Dev Biol* **12**, 697–715 (1996).

19. B. Geiger, E. Zamir, Molecular complexity and dynamics of cell-matrix adhesions. *J Cell Sci* **114**, 3577–3579 (2001).

20. R. Zaidel-Bar, S. Itzkovitz, A. Ma'ayan, R. Iyengar, B. Geiger, Functional atlas of the integrin adhesome. *Nat Cell Biol* **9**, 858–867 (2007).

21. E. R. Horton, *et al.*, Definition of a consensus integrin adhesome and its dynamics during adhesion complex assembly and disassembly. *Nat Cell Biol* **17**, 1577–1587 (2015).

22. J. D. Humphries, M. R. Chastney, J. A. Askari, M. J. Humphries, Signal transduction via integrin adhesion complexes. *Curr Opin Cell Biol* **56**, 14–21 (2019).

23. B. Z. Katz, *et al.*, Physical state of the extracellular matrix regulates the structure and molecular composition of cell-matrix adhesions. *Mol Biol Cell* **11**, 1047–1060 (2000).

24. S. Seetharaman, S. Etienne-Manneville, Integrin diversity brings specificity in mechanotransduction. *Biol Cell* **110**, 49–64 (2018).

25. O. Rossier, *et al.*, Integrins β1 and β3 exhibit distinct dynamic nanoscale organizations inside focal adhesions. *Nat Cell Biol* **14**, 1057–1067 (2012).

750 26. F. Kong, A. J. García, A. P. Mould, M. J. Humphries, C. Zhu, Demonstration of catch bonds between an integrin and its ligand. *Journal of Cell Biology* **185**, 1275–1284 (2009).

27. Y. Chen, H. Lee, H. Tong, M. Schwartz, C. Zhu, Force regulated conformational change of integrin αVβ3. *Matrix Biology* **60–61**, 70–85 (2017).

755 28. S. Huveneers, E. H. J. Danen, Adhesion signaling - Crosstalk between integrins, Src and Rho. *J Cell Sci* **122**, 1059–1069 (2009).

29. H. B. Schiller, *et al.*, β 1 - and α v -class integrins cooperate to regulate myosin II during rigidity sensing of fibronectin-based microenvironments. *Nat Cell Biol* **15**, 625–636 (2013).

760 30. C. Diaz, S. Neubauer, F. Rechenmacher, H. Kessler, D. Missirlis, Recruitment of αvβ3 integrin to α5β1 integrin-induced clusters enables focal adhesion maturation and cell spreading. *J Cell Sci* **133** (2020).

31. O. Rossier, G. Giannone, The journey of integrins and partners in a complex interactions landscape studied by super-resolution microscopy and single protein tracking. *Exp Cell*
765 *Res* **343**, 28–34 (2016).

32. T. Orré, O. Rossier, G. Giannone, The inner life of integrin adhesion sites: From single molecules to functional macromolecular complexes. *Exp Cell Res* **379**, 235–244 (2019).

33. P. Kanchanawong, *et al.*, Nanoscale architecture of integrin-based cell adhesions. *Nature* **468**, 580–584 (2010).

770 34. E. Betzig, *et al.*, Imaging intracellular fluorescent proteins at nanometer resolution. *Science (1979)* **313**, 1642–1645 (2006).

35. R. Changede, X. Xu, F. Margadant, M. P. Sheetz, Nascent Integrin Adhesions Form on All Matrix Rigidities after Integrin Activation. *Dev Cell* **35**, 614–621 (2015).

36. M. Spiess, *et al.*, Active and inactive β1 integrins segregate into distinct nanoclusters in
775 focal adhesions. *Journal of Cell Biology* **217**, 1929–1940 (2018).

37. T. K. Fujiwara, *et al.*, Ultrafast single-molecule imaging reveals focal adhesion nano-architecture and molecular dynamics. **222** (2023).

38. A. C. Chang, *et al.*, Single Molecule Force Measurements in Living Cells Reveal a Minimally Tensioned Integrin State. *ACS Nano* **10**, 10745–10752 (2016).

39. S. J. Tan, *et al.*, Regulation and dynamics of force transmission at individual cell-matrix adhesion bonds. *Sci Adv* **6**, 1–12 (2020).

40. M. Ester, H. P. Kriegel, J. Sander, X. Xu, A Density-Based Algorithm for Discovering Clusters in Large Spatial Databases with Noise. *AAAI press* 226–231 (1996).

41. S. V. Pageon, P. R. Nicovich, M. Mollazade, T. Tabarin, K. Gaus, Clus-DoC: A combined cluster detection and colocalization analysis for single-molecule localization microscopy data. *Mol Biol Cell* **27**, 3627–3636 (2016).

42. M. J. Rust, M. Bates, X. Zhuang, Sub-diffraction-limit imaging by stochastic optical reconstruction microscopy (STORM). *Nat Methods* **3**, 793–796 (2006).

43. P. Kanchanawong, D. A. Calderwood, Organization, dynamics and mechanoregulation of integrin-mediated cell–ECM adhesions. *Nat Rev Mol Cell Biol* **0123456789** (2022).

44. S. Tadokoro, *et al.*, Talin binding to integrin β tails: A final common step in integrin activation. *Science (1979)* **302**, 103–106 (2003).

45. P. Atherton, *et al.*, Relief of talin autoinhibition triggers a force-independent association with vinculin. *Journal of Cell Biology* **219** (2020).

46. N. C. Gauthier, P. Roca-Cusachs, Mechanosensing at integrin-mediated cell–matrix adhesions: from molecular to integrated mechanisms. *Curr Opin Cell Biol* **50**, 20–26 (2018).

47. J. Liu, *et al.*, Talin determines the nanoscale architecture of focal adhesions. *Proceedings of the National Academy of Sciences* **112**, E4864–E4873 (2015).

48. I. Thievessen, *et al.*, Vinculin-actin interaction couples actin retrograde flow to focal adhesions, but is dispensable for focal adhesion growth. *Journal of Cell Biology* **202**, 163–177 (2013).

49. G. J. Bakker, *et al.*, Lateral mobility of individual integrin nanoclusters orchestrates the onset for leukocyte adhesion. *Proc Natl Acad Sci U S A* **109**, 4869–4874 (2012).

50. T. S. van Zanten, *et al.*, Hotspots of GPI-anchored proteins and integrin nanoclusters function as nucleation sites for cell adhesion. *Proc Natl Acad Sci U S A* **106**, 18557–18562 (2009).

51. A. Cambi, *et al.*, Organization of the Integrin LFA-1 in Nanoclusters Regulates Its Activity. *Mol Biol Cell* **17**, 4270–4281 (2006).

810 52. S. J. Han, *et al.*, Pre-complexation of talin and vinculin without tension is required for efficient nascent adhesion maturation. *Elife* **10**, 1–29 (2021).

53. J. C. Friedland, M. H. Lee, D. Boettiger, Mechanically activated integrin switch controls α5β 1 function. *Science (1979)* **323**, 642–644 (2009).

54. P. Atherton, *et al.*, Tensin3 interaction with talin drives the formation of fibronectin-
815 associated fibrillar adhesions. *Journal of Cell Biology* **221** (2022).

55. F. Margadant, *et al.*, Mechanotransduction in vivo by repeated talin stretch-relaxation events depends upon vinculin. *PLoS Biol* **9** (2011).

56. Z. Sun, *et al.*, Kank2 activates talin, reduces force transduction across integrins and induces central adhesion formation. *Nat Cell Biol* **18**, 941–953 (2016).

820 57. B. P. Bouchet, *et al.*, Talin-KANK1 interaction controls the recruitment of cortical microtubule stabilizing complexes to focal adhesions. *Elife* **5**, 1–23 (2016).

58. M. Yu, *et al.*, Force-Dependent Regulation of Talin-KANK1 Complex at Focal Adhesions. *Nano Lett* **19**, 5982–5990 (2019).

59. K. Guo, *et al.*, KANK1 shapes focal adhesions by orchestrating protein binding,
825 mechanical force sensing, and phase separation. *Cell Rep* **42**, 113321 (2023).

60. L. B. Case, M. De Pasquale, L. Henry, M. K. Rosen, Synergistic phase separation of two pathways promotes integrin clustering and nascent adhesion formation. *Elife* **11**, 1–36 (2022).

61. B. Huang, W. Wang, M. Bates, X. Zhuang, Three-dimensional super-resolution imaging
830 by stochastic optical reconstruction microscopy. *Science (1979)* **319**, 810–813 (2008).

62. A. Dani, B. Huang, J. Bergan, C. Dulac, X. Zhuang, Superresolution Imaging of Chemical Synapses in the Brain. *Neuron* **68**, 843–856 (2010).

63. M. Lelek, *et al.*, Single-molecule localization microscopy. *Nature Reviews Methods Primers* **1** (2021).

835 64. J. Schindelin, *et al.*, Fiji: An open-source platform for biological-image analysis. *Nat Methods* **9**, 676–682 (2012).